Electronic Supplementary Material (ESI) for Chemical Science.

Supporting Information for

Core-Dependent Properties of Copper Nanoclusters: Valence-Pure Nanoclusters as NIR TADF Emitters and Mixed-Valence Ones as Semiconductors

I. Experimental Section

Chemicals and reagents: All chemicals and reagents were commercially available and used as received. 3-Methyl-1-butyne (^{i}PrC≡CH, 96%) was purchased from Alfa Aesar; 3,3-dimethyl-1-butyne (^{t}BuC≡CH, 97%) was purchased from International Laboratory USA; *tert*-butylphosphonic acid ($^{t}BuPO_3H_2$, 98%) was purchased from Acros Organics; sodium orthovanadate (Na_3VO_4, 98%) was purchased from Farco Chemical Supplies.

Instrumentation: Elemental analyses (C and H) were performed on a Perkin-Elmer 2400 elemental analyzer. IR spectra were recorded in the range 400−4000 cm^{-1} on a Nicolet Impact 420 FTIR spectrometer with pressed KBr pellets. Powder X-ray diffraction (PXRD) were performed using a Rigaku SmartLab X-ray diffractometer (Cu*K*α radiation). Energy dispersive X-ray spectroscopy (EDS) analysis was performed on a JEOL JSM6700F field-emission scanning electron microscope equipped with an Oxford INCA system. Thermogravimetric analysis (TGA) was carried out on a Mettler Toledo TGA/SDTA 851e analyzer at a ramp rate of 10 ºC/min from 50 to 800 ºC. Electron paramagnetic resonance (EPR) data of **3** and **4** were recorded on a Bruker EMX-EPR Spectrometer at T = 7 K in the solid state. UV-Vis-NIR diffuse reflectance was recorded using finely ground powder samples with $BaSO_4$ as standard on a SHIMADZU UV-3600 spectrophotometer. Temperature-dependent emission spectra and lifetimes were recorded using a FLS980 Edinburgh spectrometer equipped with an OptistatDN2 cryostat. The recording temperature range for **1** and **2** was 77−398 K and 77−328 K, respectively. The upper temperature limits are lower than the thermal stability temperature of **1** and **2** (423 K) since the emission intensity above such temperature became very weak. The excitation and emission spectra were processed with standard corrections to eliminate the influence of the excitation source and the sensitivity of the detector. Decay lifetimes were measured using a μF900 pulsed Xenon microsecond flash lamp with instrumental response function (IRF) applied.

Syntheses:

$[Cu(I)_{15}(^{t}BuC{\equiv}C)_{14}NO_3]$ (1)

To a 250-ml round-bottom flask, $Cu(II)(NO_3)_2{\cdot}3H_2O$ (0.50 mmol, 0.121 g), copper powder Cu(0) (0.127 g, 2.00 mmol), ^{t}BuC≡CH (0.5 ml, 4.06 mmol) and methanol (10 mL) were added. This flask was capped with a stopper and sealed with parafilm. The reaction mixture was stirred overnight to give a red solution. This crude solution was filtered, and red crystals of **1** were obtained by storing the filtrate at −20°C within

a few days. After removing the crystals by filtration, a second batch was collected to give a final yield of 80%. Yield: 0.114 g (80%, based on Cu(II)). Elemental analysis (%) for **1** as $C_{84}H_{126}Cu_{15}NO_3$, found (calcd): C, 46.94 (46.90); H, 5.88 (5.90). Infrared (KBr, cm^{-1}): NO_3: 1358 (m); 886 (w).

$[Cu(I)_{28}(^tBuC{\equiv}C)_{22}(SO_4)_2(OCH_3)_2]$ (2)

To a 250-ml round-bottom flask, Cu(II)SO_4 (0.080 g, 0.50 mmol), copper powder Cu(0) (0.127 g, 2.00 mmol), ^{t}BuC≡CH (0.5 ml, 4.06 mmol) and methanol (10 mL) were added. This flask was capped with a stopper and sealed with parafilm. The reaction mixture was stirred overnight at 60°C to give a yellow-orange precipitate. To dissolve the precipitate, an amount of *ca.* 50 ml methanol was added, and heated under stirring at 100°C for 2 hours to give a clear red solution. Upon filtration, the filtrate was transferred to a glass bottle and stored at −20°C to yield yellow crystals of **2** within two months. Before appearance of crystals, we would rotate the bottle gently and then put it back to the refrigerator. And once we saw crystals, we would repeat such manipulation to increase the crystal yield. Yield: 0.02 g (14.6%, based on Cu(II)). Elemental analysis (%) for **2** as $C_{134}H_{204}Cu_{28}O_{10}S_2$, found (calcd): C, 41.95 (42.15); H, 5.38 (5.38). Infrared (KBr, cm^{-1}): SO_4^{2-}: 1122 (m); 622 (w).

$\{[Cu(II)O_6]@Cu(I)_{47}(^iPrC{\equiv}C)_{33}\}\cdot(ClO_4)_4$ (3)

To a 250-ml round-bottom flask, ^{t}BuPO_3H_2 (0.020 g, 0.145 mmol), Na_3VO_4 (0.020 g, 0.11 mmol) and a small amount of 0.3 ml H_2O was added, followed by addition of Cu(II)$(ClO_4)_2\cdot 6H_2O$ (0.30 mmol, 0.111 g), copper powder Cu(0) (0.127 g, 2.00 mmol), ^{i}PrC≡CH (0.5 ml, 4.89 mmol), and methanol (10 mL). This flask was capped with a stopper and sealed with parafilm. The reaction mixture was vigorously stirred overnight at room temperature to give a yellow precipitate. The precipitate was subsequently collected by filtration, and re-dissolved in CH_2Cl_2 under stirring. Slow diffusion of Et_2O into the CH_2Cl_2 filtrate yielded deep red crystals of **3** after two weeks. Yield: 0.015 g (21%, based on Cu(II)). Elemental analysis (%) for **3** as $C_{165}H_{231}Cl_4Cu_{48}O_{22}$ (after removal of solvent molecules under vacuum), found (calcd): C, 34.36 (34.41); H, 4.02 (4.04).

$\{[Cu(II)O_4]\cdot[VO_4]_2@Cu(I)_{46}(^tBuC{\equiv}C)_{27}(^tBuPO_3)_2(H_2O)\}\cdot(BF_4)_3\cdot(CH_2Cl_2)_2\cdot(Et_2O)_2\cdot(H_2O)$ (4)

To a 250-ml round-bottom flask, ^{t}BuPO_3H_2 (0.020 g, 0.145 mmol), Na_3VO_4 (0.020 g, 0.11 mmol) and a small amount of 0.3 ml H_2O was added, followed by addition of Cu(II)$(BF_4)_2\cdot xH_2O$ (*ca.* 0.50 mmol, 0.118 g), copper powder Cu(0) (0.127 g, 2.00 mmol), ^{t}BuC≡CH (0.5 ml, 4.06 mmol), and methanol (10 mL). The reaction mixture was vigorously stirred overnight at room temperature (alternatively, upon gentle stirring at 60°C) to yield a red precipitate. This red precipitate was collected by filtration and re-

dissolved in CH_2Cl_2 under stirring. Slow diffusion of Et_2O into the CH_2Cl_2 filtrate yielded black-brown crystals of **4** after two weeks. Yield: 0.035 g (26%, based on Cu(II)). Elemental analysis (%) calcd for **4** as $C_{170}H_{263}B_3F_{12}P_2V_2Cu_{47}O_{19}$ (after removal of solvent molecules under vacuum), found (calcd): C, 34.07 (33.95); H, 4.34 (4.40).

Vanadate-induced formation of the incorporating Cu(II) cation in 3 and 4:

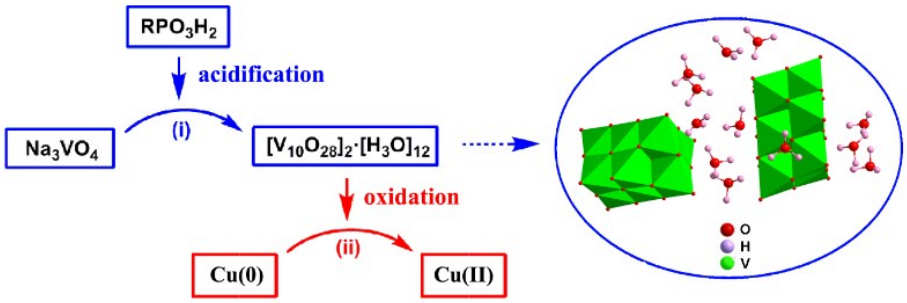

Scheme S1. Proposed mechanism for vanadate-induced formation of the incorporating Cu(II) cation in **3** and **4**. Step i) Na_3VO_4 upon acidification by $^tBuPO_3H_2$ formed the intermediate $[V_{10}O_{28}]_2{\cdot}[H_3O]_{12}$, with its X-ray structure shown inside an oval; Step ii) $[V_{10}O_{28}]_2{\cdot}[H_3O]_{12}$-triggered oxidation of Cu(0) to in situ generate the Cu(II) cation.

Based on comproportionation reaction to form Cu(I) nanoclusters, the addendum unit of $Na_3VO_4/^tBuPO_3H_2$ was introduced to furnish the Cu(II)-incorporated Cu(I) nanoclusters **3** and **4**. By conducting control experiments, it is postulated that the Cu(II) cation was in situ generated stepwisely, as shown in Scheme S1. Firstly, Na_3VO_4 upon acidification by $^tBuPO_3H_2$ to form a crucial intermediate $[V_{10}O_{28}]_2{\cdot}[H_3O]_{12}$ (Fig. S13), which is in accordance with the reaction $20Na_3VO_4 + 30^tBuPO_3H_2 = [V_{10}O_{28}]_2{\cdot}[H_3O]_{12} + 30Na_2{}^tBuPO_3 + 12H_2O$. As observed, Na_3VO_4 (white color) and $^tBuPO_3H_2$ (white color) upon mixing in the solid state immediately turned an orange solid. Dissolving of the orange solid by water and methanol (3: 1) gave an orange solution, which upon evaporation deposited orange crystals of $[V_{10}O_{28}]_2{\cdot}[H_3O]_{12}$ in good yield. This reaction is in accord to the common knowledge that the vanadate anion upon acidification transforms to polyoxovanadate species. Notably, this hydronium decavanadate compound $[V_{10}O_{28}]_2{\cdot}[H_3O]_{12}$ has not been reported prior to this work. Furthermore, $^tBuPO_3H_2$ can be replaced by $PrPO_3H_2$ or $PhPO_3H_2$, suggesting that the general role of RPO_3H_2 is providing protons to form $[V_{10}O_{28}]_2{\cdot}[H_3O]_{12}$. Subsequently, Cu(0) upon oxidation by $[V_{10}O_{28}]_2{\cdot}[H_3O]_{12}$ in situ generated the Cu(II)

cation. Herein, addition of Cu(0) to Na_3VO_4/^{t}BuPO$_3$H$_2$ solution soon led to dissolution of the copper powder, accompanied by solution color change from range to deep blue. Evaporation of this solution afforded tiny blue crystals not suitable for X-ray diffraction analysis. Nevertheless, replacing ^{t}BuPO$_3$H$_2$ with PrPO$_3$H$_2$ allowed us to grow good single crystals, which was crystallographically characterized as [Cu(II)(PrPO$_3$)(H$_2$O)]$_n$ (Fig. S14).[1] This control experiment confirmed that Na_3VO_4/^{t}BuPO$_3$H$_2$ triggered oxidation of Cu(0) to Cu(II). In addition, **3** can be accomplished by direct introduction of $[V_{10}O_{28}]_2 \cdot [H_3O]_{12}$ into the comproportionation reaction, which further suggests the essential role of this intermediate in synthesis of **3** and **4**.

II. Spectrometric Characterizations

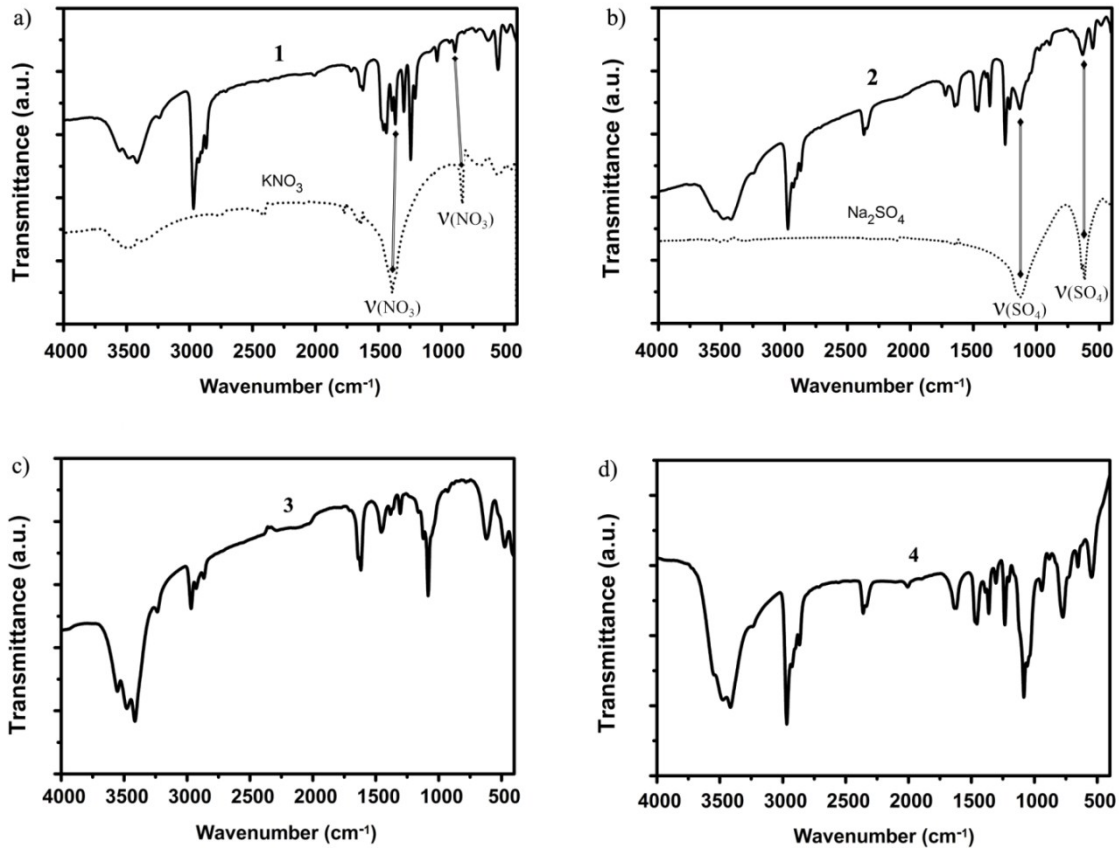

Fig. S1 IR spectra of a) **1**, b) **2**, c) **3**, and d) **4**. KNO_3 and Na_2SO_4 (dashed line) were used as references to identify the vibration frequency of NO_3^- and SO_4^{2-} in **1** and **2**, respectively, which are marked by the double-head arrow.

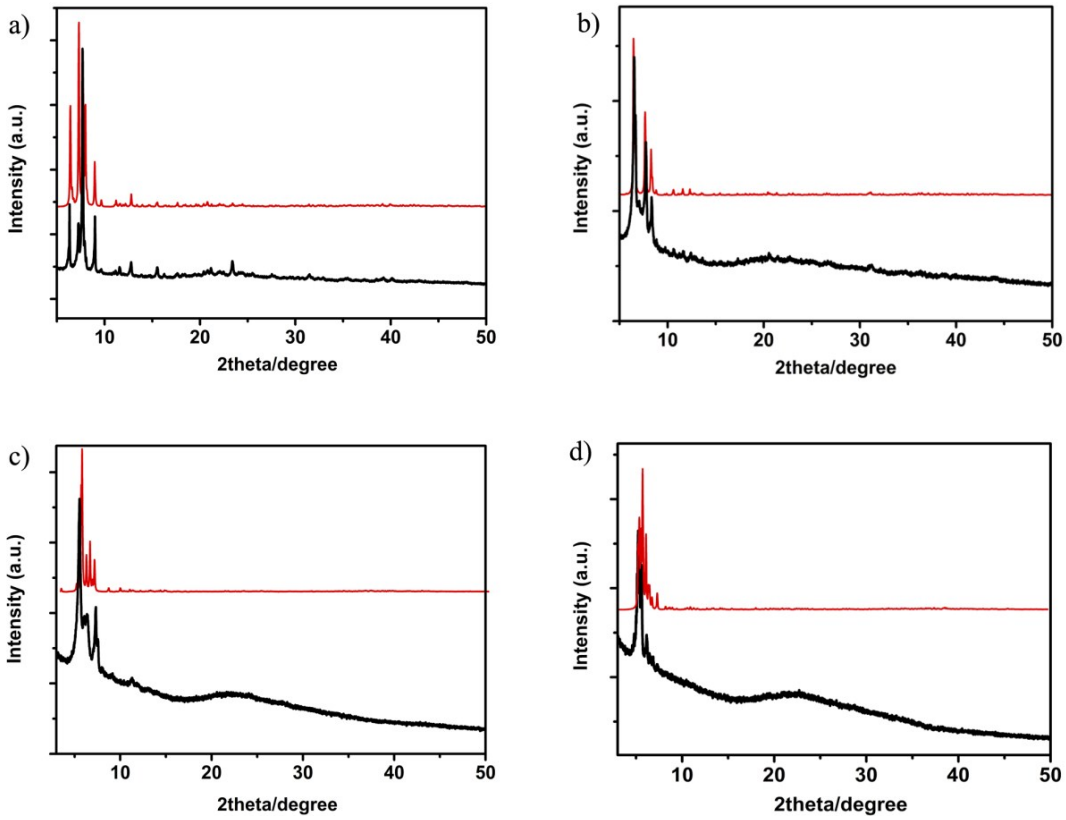

Fig. S2 Simulated (red line) and experimental (black line) PXRD patterns of a) **1**, b) **2**, c) **3**, and d) **4**.

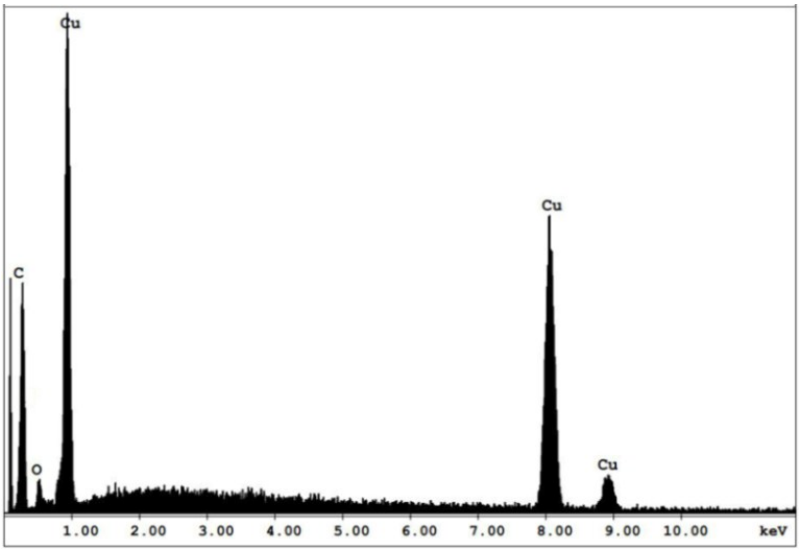

Fig. S3 EDS spectrum of **1**. The signal of nitrogen is absent since its response is too weak to be detected for most common EDS detector designs.[2]

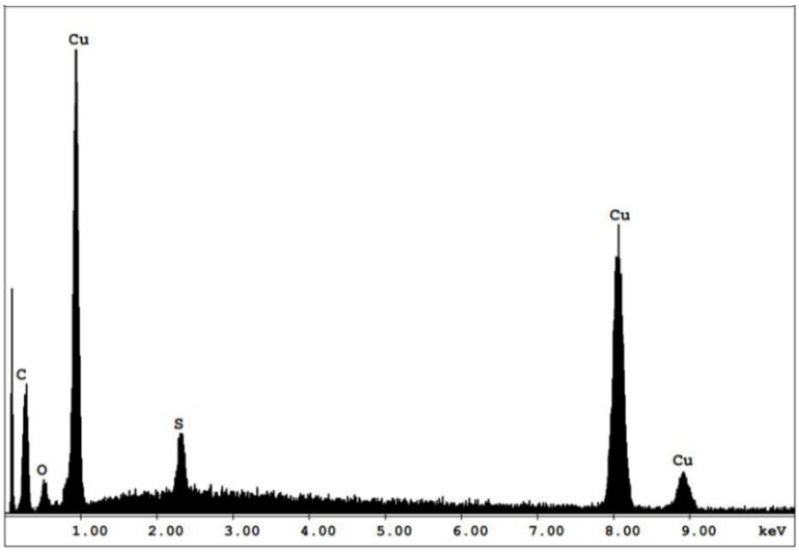

Fig. S4 EDS spectrum of **2**.

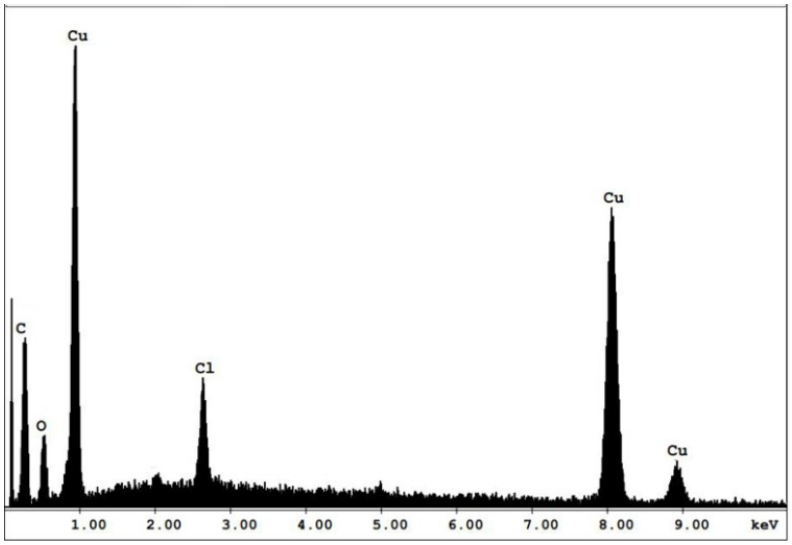

Fig. S5 EDS spectrum of **3**.

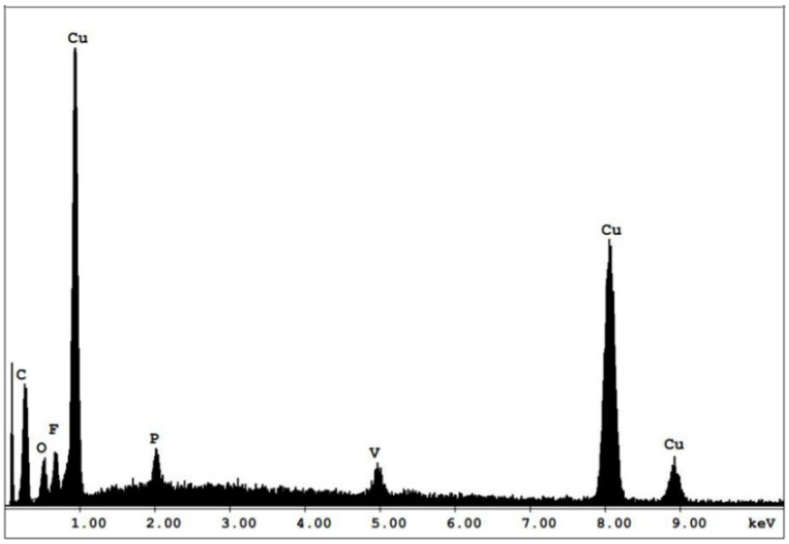

Fig. S6 EDS spectrum of **4**.

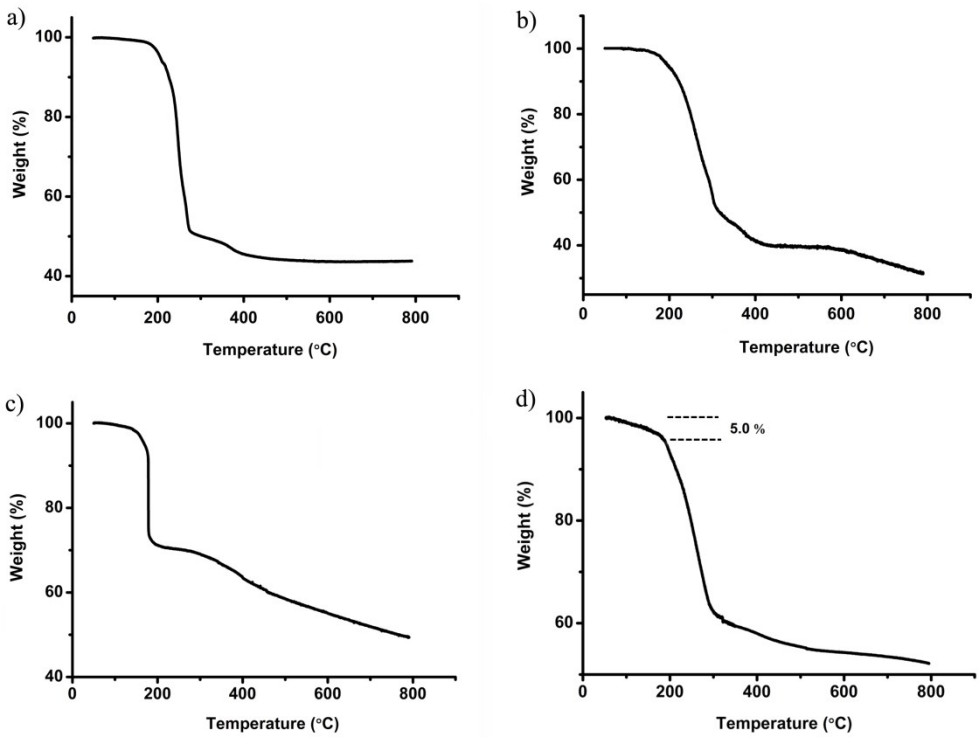

Fig. S7 TGA curves of a) **1**, b) **2**, c) **3**, and d) **4**. In d), the weight loss of 5.0% corresponds to evacuation of the solvent molecules $2Et_2O + 2CH_2Cl_2 + H_2O$ (calc. 5.28%) in **4**. TGA analysis confirmed that **1**−**4** are thermally stable to about 150 °C.

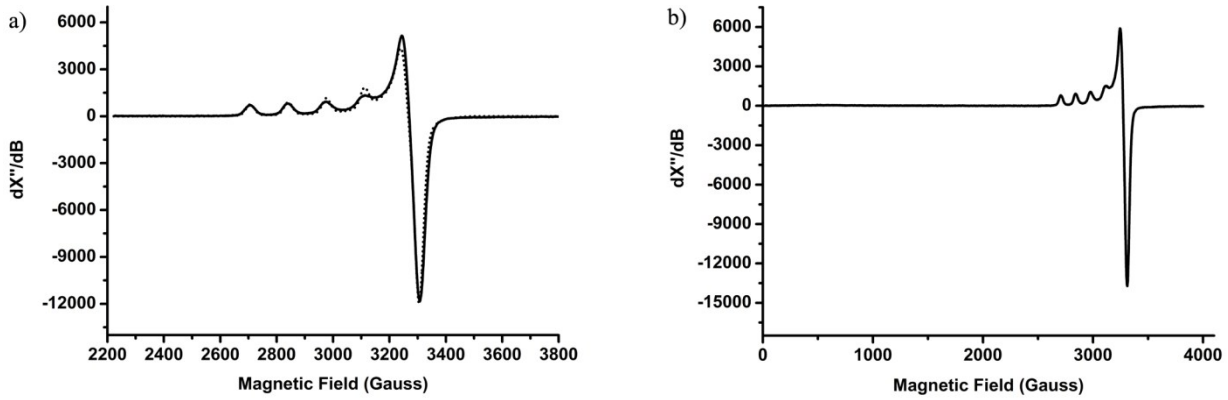

Fig. S8 a) EPR spectrum of **3** recorded at T = 7 K in the solid state. Spectral parameters: $g_{//}$ = 2.310, $g_{\perp}$ = 2.053; hyperfine coupling to Cu(II) (I = 3/2): $A_{//}$ = 135 Gauss, $A_{\perp}$ = 11.1 Gauss. Solid line: experimental; dashed line: simulated. b) EPR spectrum in the range 0−4000 Gauss at T = 7 K. No response in mid-field (1500~2000 Gauss) region signifies the absence of Cu(II)···Cu(II) interaction, and in the present case it indicates the presence of a single Cu(II) cation.

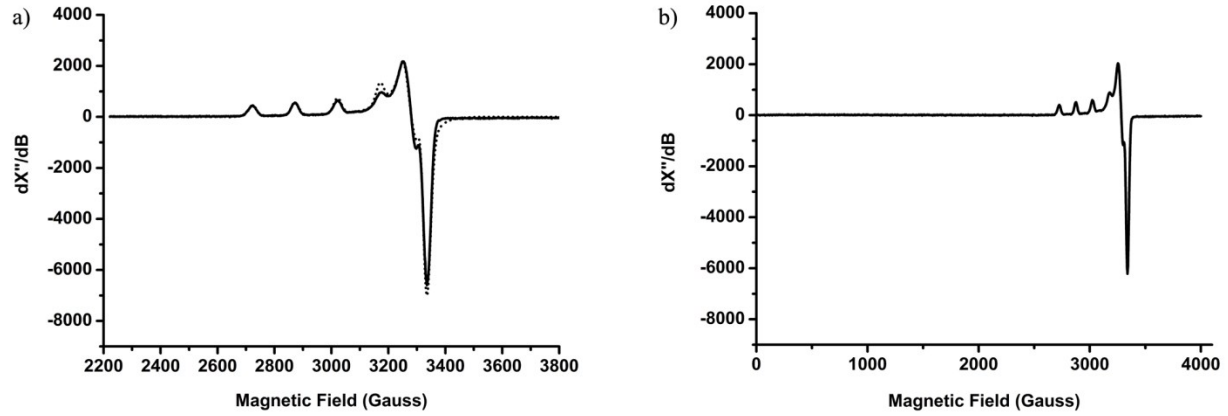

Fig. S9 a) EPR spectrum of **4** recorded at T = 7 K in the solid state. Spectral parameters: $g_{//}$ = 2.280, $g_{\perp}$ = 2.040; hyperfine coupling to Cu(II) (I = 3/2): $A_{//}$ = 150 Gauss, $A_{\perp}$ = 16.0 Gauss. Solid line: experimental; dashed line: simulated. b) EPR spectrum recorded in the range 0−4000 Gauss at T = 7 K. No response in mid-field (1500~2000 Gauss) region signifies the absence of Cu(II)···Cu(II) interaction, and in the present case it indicates the presence of a single Cu(II) cation.

III. Dielectric and Conductivity Measurements:

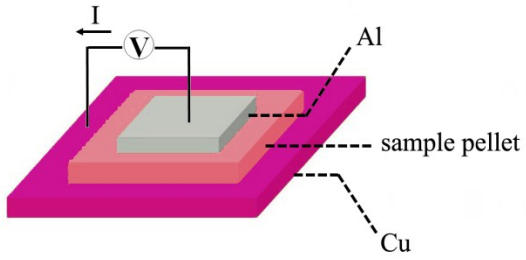

Fig. S10 Electronic device used for dielectric and conductivity measurement.

To prepare the sample pellets of **1**–**4**, about 15 mg of bulk crystals were ground in an agate mortar. The finely ground powders were transferred to the central section of a Cu metal sheet with an area of 1.0 cm × 1.0 cm. Afterwards a tiny piece of weighing paper was used to cover the powders and then compressed by a pressing equipment (e.g. one used in IR measurement) at a pressure of 5 tons for a few seconds. Upon gentle removal of the weighing paper, a compact sample pellet was affixed on the Cu metal sheet. The thickness and area of the pellet were measured by a micrometer. Finally, this composite was coated with a thin Al metal layer via thermal evaporation method, where the pattern of the Al layer was controlled by a shadow mask with a feature size (ca. 2.5 mm × 2.5 mm). Fig. S10 shows the final structure of the electronic device where the area of the component should follow the order: Al layer < sample pellet < Cu sheet. Dielectric measurement was conducted on an Agilent 4263B LCR Meter equipment. Temperature-dependent electrical conductivity was measured by recording current–voltage (I–V) curve using a Keithley sourcemeter 2612 equipment to scan the current on a voltage basis of −5 to 5 V. Temperature was control by Cryogenic Stage (Linkam T95-PE) and at every temperature step, a soak time of 2 minutes was generally required. The conductivity was extracted from linear regression results of the I–V curves. The activation energy was determined by fitting with the Arrhenius equation, $\sigma = \sigma_0 e^{-Ea/(k*T)}$, where σ_0 is the conductivity prefactor, Ea the activation energy, k the Boltzmann constant, and T the temperature. The experimental conductivity was recorded in the range 293–373 K where above 373 K the Al layer became crispy and started to crack.

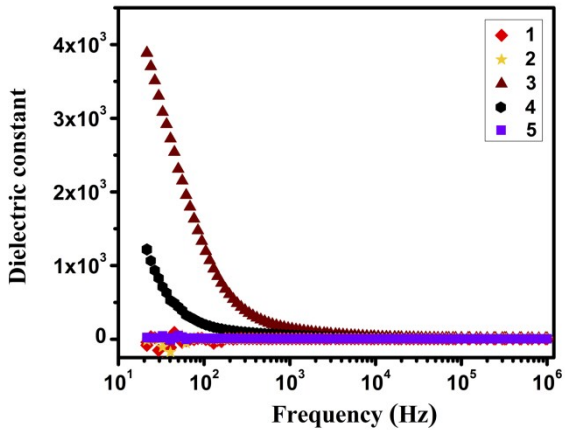

Fig. S11 Frequency-dependent dielectric behavior of **1**–**5**. Herein, **5** represents the previously reported complex $[Cu(I)_{17}(^{t}BuC{\equiv}C)_{16}MeOH]\cdot BF_4$ comprising the cationic cluster of $[Cu(I)_{17}(^{t}BuC{\equiv}C)_{16}MeOH]^{+}$ and the BF_4^{-} counter anion.[3]

IV. Crystal Structures

Single-Crystal X-ray Diffraction: Crystallographic data of **1**−**4** were collected at a temperature of 173 K on a single crystal diffractometer using graphite-monochromatic Mo Kα radiation (λ = 0.71073 Å). All structures were solved by direct methods and refined with the full-matrix least-squares technique based on F^2 using SHELXTL.[4] All non-hydrogen atoms were refined anisotropically, and hydrogen atoms bonded to carbon were generated geometrically. Compound **3** has a solvent accessible area of 13.3% per unit-cell (5499.0/41500.0 Å^3), in which the solvent molecules (CH_2Cl_2 and Et_2O) are highly disordered to be unambiguously modeled. *SQUEEZE* program implemented in *PLATON* was applied to remove solvent electron density (*SQUEEZE* result has been appended to cif file).[5] Furthermore, these solvent molecules evacuate from the crystal lattice at room temperature, which gave unsatisfactory TGA and EA results. Therefore, TGA and EA measurements of **3** were performed on crystal samples after removing the solvent molecules under vacuum by stirring.

For compound $[V_{10}O_{28}]_2 \cdot [H_3O]_{12}$, hydrogen atoms riding on oxygen were all found on the difference Fourier map, brought to reasonable distances from their parent oxygen atoms, and then fixed. Crystallographic data for $[V_{10}O_{28}]_2 \cdot [H_3O]_{12}$: triclinic, space group $P\bar{1}$, a = 10.1593(8) Å, b = 10.2950(9) Å, c = 16.7352(13) Å, α = 83.426(2)°, β = 87.127(2)°, γ = 71.045(2)°, V = 1644.4(2) Å^3, T = 296 K, Z = 2, R_1 = 0.0346 for reflections with $I > 2\sigma(I)$, wR_2 = 0.1049 for all data, number of reflections/unique reflections = 52059/7911, GOF = 1.207, CCDC no. 1907669. Crystallographic data for $[Cu(II)(PrPO_3)(H_2O)]_n$: monoclinic, space group $P2_1/c$, a = 11.9726(15) Å, b = 7.5977(10) Å, c = 7.4217(9) Å, α = 90°, β = 97.625(4)°, γ = 90°, V = 669.14(15) Å^3, T = 296 K, Z = 4, R_1 = 0.1177 for reflections with $I > 2\sigma(I)$, wR_2 = 0.3087 for all data, number of reflections/unique reflections = 12755/1464, GOF = 1.210, CCDC no. 1907707.

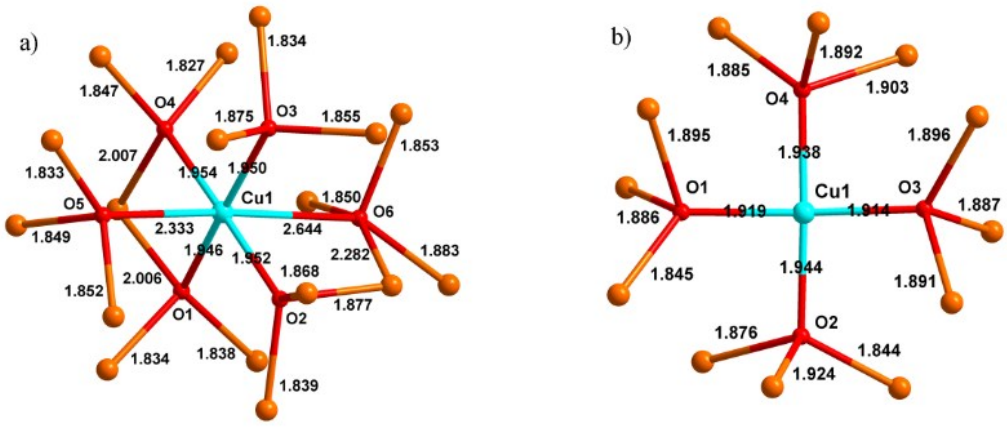

Fig. S12 Cu(I)–O–Cu(II) bonding interactions in a) **3** and b) **4** with the bond distances shown. In **3**, Cu1 exhibits an octahedral coordination environment with significant Jahn-Teller distortion, whereas in **4** Cu1 displays a distorted square-planar coordination geometry.

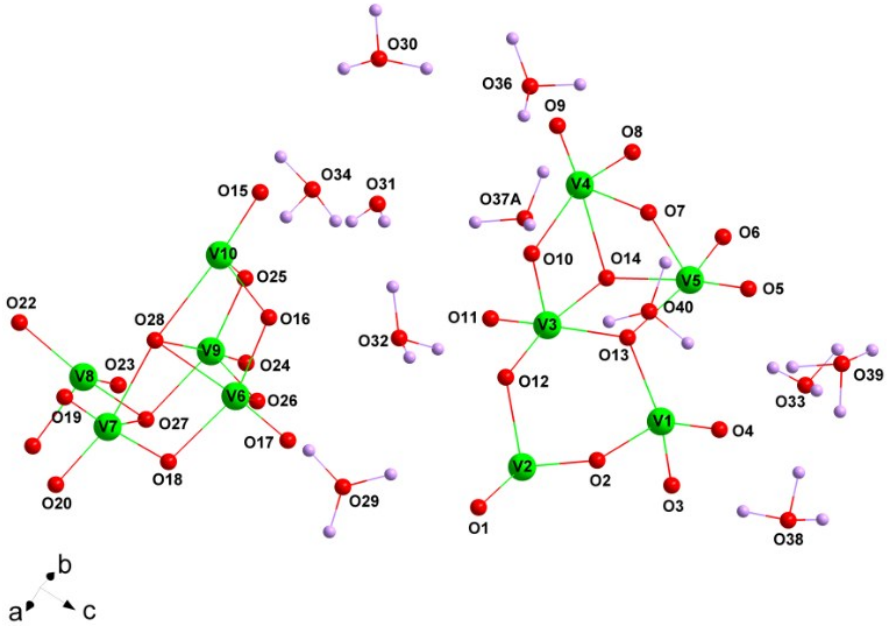

Fig. S13 Asymmetric unit of $[V_{10}O_{28}]_2 \cdot [H_3O]_{12}$ with atom labels shown. Color code: V−green, O−red, and H−rose.

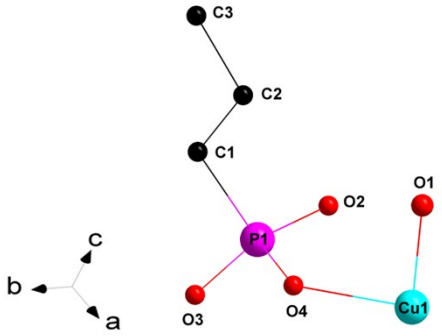

Fig. S14 Asymmetric unit of $[Cu(II)(PrPO_3)(H_2O)]_n$ with atom labels shown.

Table S1. Crystallographic data of **1**−**4**.

Compound	**1**	**2**	**3**	**4**
CCDC no.	1907665	1907666	1907667	1907668
Formula	$C_{84}H_{126}Cu_{15}NO_3$	$C_{134}H_{204}Cu_{28}O_{10}S_2$	$C_{165}H_{231}Cl_4Cu_{48}O_{22}$	$C_{180}H_{289}B_3Cl_4Cu_{47}F_{12}O_{22}P_2V_2$
M_r	3818.47	3818.47	5758.60	6357.92
Crystal system	monoclinic	monoclinic	monoclinic	triclinic
Space group	$C2/c$	$P2_1/c$	$C2/c$	$P\bar{1}$
a (Å)	49.115(10)	18.680(2)	56.4611(18)	19.9192(17)
b (Å)	15.305(3)	14.6314(17)	19.3733(7)	20.0207(17)
c (Å)	28.157(5)	31.316(4)	38.1762(13)	32.564(3)
α (°)	90	90	90	90.482(2)
β (°)	112.054(10)	104.937(3)	96.377(2)	101.813(2)
γ (°)	90	90	90	116.372(2)
V (Å^3)	19617(7)	8269.9(17)	41500(2)	11315.2(17)
T(K)	173	173	173	173
Z	8	2	8	2
D_{calcd} (g cm^{-3})	1.420	1.490	1.833	1.855
μ (mm^{-1})	3.215	3.580	4.898	4.507
F(000)	8336.0	3648.0	22656.0	6278.5
Reflns	67408	182816	191889	162295
Unique reflns	21404	20477	38009	39875
GOF	1.000	1.037	1.074	1.115
R_{int}	0.1321	0.1144	0.0750	0.0436
R_1 [$I > 2\sigma(I)$][a]	0.0801	0.0761	0.0610	0.0681
wR_2 (all data)[b]	0.2704	0.2144	0.1936	0.1920

[a]$R_1=\sum||F_0|-|F_c||/\sum|F_0|$; [b]$wR_2=\{\sum[w(F_0^2-F_c^2)^2]/\sum w(F_0^2)^2\}^{1/2}$.

Table S2. Bond-valence sum (BVS)[6] calculations for **3** and **4**.

3			**4**		
bond	length (Å)	BVS	bond	length (Å)	BVS
Cu1–O1	1.957	0.471729	Cu1–O1	1.918	0.524166
Cu1–O2	1.940	0.493908	Cu1–O2	1.945	0.487279
Cu1–O3	1.947	0.484652	Cu1–O3	1.913	0.531298
Cu1–O4	1.950	0.480738	Cu1–O4	1.940	0.493908
Cu1–O5	2.325	0.174574			sum: **2.04**
Cu1–O6	2.635	0.075549	V1–O5	1.730	1.218106
		sum: **2.18**	V1–O6	1.771	1.090337
			V1–O7	1.717	1.261665
			V1–O8	1.719	1.254864
					sum: **4.80**
			V2–O9	1.723	1.241371
			V2–O10	1.698	1.328146
			V2–O11	1.766	1.105171
			V2–O12	1.712	1.27883
					sum: **4.95**

V. References

[1] S. Chausson, J.-M. Rueff, M. B. Lepetit, O. Perez, R. Retoux, C. Simon, L. L. Pluart, P.-A. Jaffrès, *Eur. J. Inorg. Chem.* **2012**, 2193.

[2] J. Berlin, T. Salge, M. Falke, D. Goran, Recent Advances in EDS and EBSD Technology: Revolutionizing the Chemical Analysis of Chondritic Meteorites at the Micro- and Nanometer Scale, 42nd Lunar and Planetary Science Conference, 2723, (2011).

[3] L.-M. Zhang, T. C. W. Mak, *J. Am. Chem. Soc.* **2016**, *138*, 2909.

[4] C. B. Hübschle, G. M. Sheldrick, B. Dittrich, *J. Appl. Cryst*. **2011**, *44*, 1281.

[5] A. L. Spek, *J. Appl. Crystallogr*. **2003**, *36*, 7.

[6] I. D. Brown, D. Altermatt, *Acta Crystallogr.* **1985**, *B41*, 244.